RESEARCH LETTER

InSAR observations of strain accumulation and fault creep along the Chaman Fault system, Pakistan and Afghanistan

Heresh Fattahi[1,2] and Falk Amelung[2]

[1]Rosenstiel School of Marine and Atmospheric Science, University of Miami, Coral Gables, Florida, USA, [2]Now at Seismological Laboratory, California Institute of Technology, Pasadena, California, USA

Abstract We use 2004–2011 Envisat synthetic aperture radar imagery and InSAR time series methods to estimate the contemporary rates of strain accumulation in the Chaman Fault system in Pakistan and Afghanistan. At 29 N we find long-term slip rates of 16 ± 2.3 mm/yr for the Ghazaband Fault and of 8 ± 3.1 mm/yr for the Chaman Fault. This makes the Ghazaband Fault one of the most hazardous faults of the plate boundary zone. We further identify a 340 km long segment displaying aseismic surface creep along the Chaman Fault, with maximum surface creep rate of 8.1 ± 2 mm/yr. The observation that the Chaman Fault accommodates only 30% of the relative plate motion between India and Eurasia implies that the remainder is accommodated south and east of the Katawaz block microplate.

1. Introduction

The earthquake potential along the western India plate boundary depends on whether the relative plate motion between the India and Eurasia plates localizes along one major plate bounding fault or is distributed over multiple faults or a broader zone [*Thatcher*, 2009; *Molnar and Dayem*, 2010] and on the degree of seismic coupling [e.g., *Avouac*, 2015]. Early and recent geologic studies suggest that most or all of the plate motion is accommodated along the Chaman Fault [*Yeats et al.*, 1979; *Lawrence et al.*, 1992; *Ul-Hadi et al.*, 2013]. In contrast, sparse GPS data suggest partitioning of the plate boundary deformation between the Chaman and Ghazaband Faults [*Szeliga et al.*, 2012]. No geodetic observation of aseismic creep has been reported for Chaman and Ghazaband Faults except for aseismic afterslip following moderate earthquakes by *Furuya and Satyabala* [2008] and *Fattahi et al.* [2015].

The Ghazaband Fault threatens the city of Quetta, the capital of Balochistan province, which was last destroyed by an earthquake in 1935, causing 35,000 fatalities [*Ambraseys and Bilham*, 2003]. The northern Chaman Fault poses a hazard for the city of Kabul, which was last destroyed by an earthquake in 1505 [*Bernard et al.*, 2000; *Ambraseys and Bilham*, 2003; *Szeliga et al.*, 2012; *Yeats*, 2012]. Here we use 7 years of interferometric synthetic aperture radar (InSAR) data to derive constraints on the long-term slip rates and on the seismic potential of the faults in the region.

2. Geologic Setting

The western Indian plate boundary is a complex, transpressional zone accommodating 29 mm/yr relative plate motion between the India and Eurasia plates (Figure 1a). The shear component is accommodated by the Chaman Fault system, which is worldwide one of the longest (~1200 km) continental strike-slip systems. The shortening component is accommodated by the thrust faults in the Kirthar Range, Sulaiman Lobe, and Sulaiman Range [*Haq and Davis*, 1997; *Bernard et al.*, 2000]. The Chaman Fault system consists of the Ornach Nal Fault which runs from the offshore triple junction to a latitude of ~28 N, the Ghazaband Fault which runs to the town of Pishin, and the Chaman Fault proper, which runs from latitude N28.25 where the arcuate faults of the Makran Range merge parallel to the Ghazaband Fault up to its namesake city of Chaman, which was destroyed by the 1892 earthquake, and then to the Herat Fault. The widening of the plate boundary zone north of Quetta has been attributed to the rigid Katawaz block [*Haq and Davis*, 1997; *Bernard et al.*, 2000; *Ambraseys and Bilham*, 2003]. During the last century the plate boundary zone generated four $M > 7$ earthquakes including the 1909 M7.1 Kachhi [*Ambraseys and Bilham*, 2003], the 1931 M7.3 Mach [*Szeliga et al.*, 2009], the 1935 M7.7 Quetta [*Armbruster et al.*, 1980], and the 2013 M7.7 Balochistan earthquakes [*Avouac et al.*, 2014].
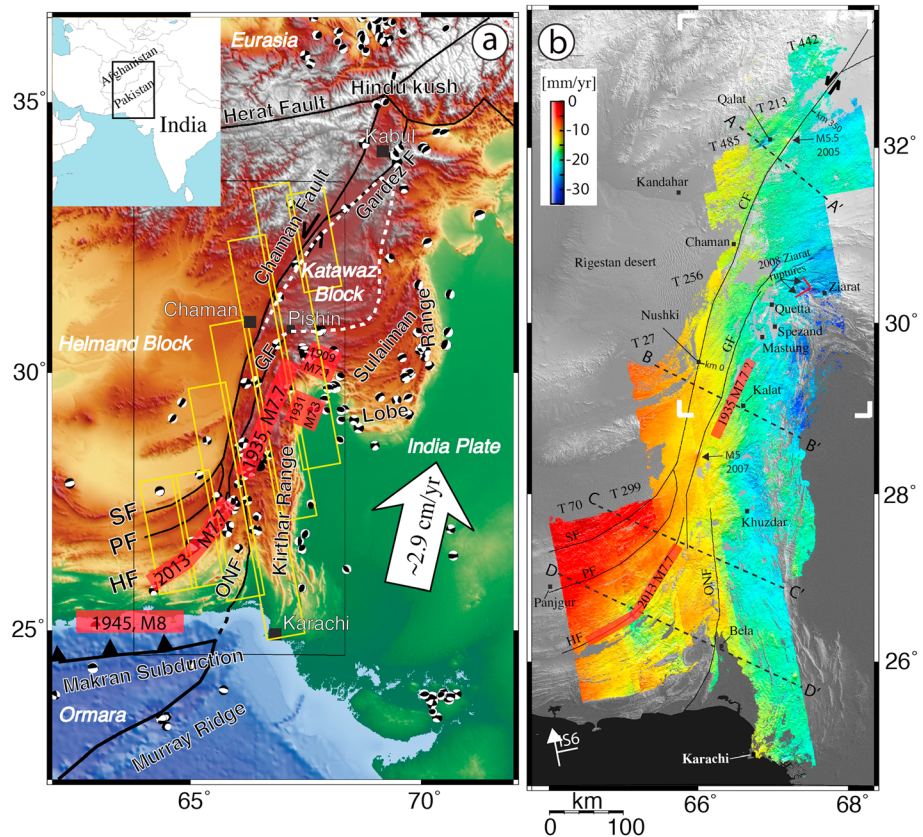
Figure 1. (a) Western India plate boundary zone and (b) InSAR LOS velocity field obtained from seven ascending tracks of Envisat ASAR data. Black rectangle in Figure 1a: location of Figure 1b; dashed lines in Figure 1b: transects. GF: Ghazaband Fault, HF: Hoshab Fault, PF: Panjgur Fault, SF: Siahan Fault, ONF: Ornach Nal Fault. The focal mechanisms are from the Global CMT catalog. The relative motion between India and Eurasia is for Sukkur Pakistan (27.69°N, 68.84°E) using International Terrestrial Reference Frame 2008. The relative motion between the Helmand block and Eurasia is small to negligible[24]. The inconsistencies between adjacent tracks at 26°N–27°N are the result of a bias due to the residual tropospheric delay caused by the inaccuracy of the atmospheric model.

3. InSAR Data and Processing Approach

We use ~2004 to ~2011 ascending Envisat advanced synthetic aperture radar (ASAR) data from tracks 70, 299, 27, 256, 485, 213, and 442 (beam IS6) and descending ASAR data from track 134 (beam IS2). We generate zero Doppler single look complex images using the synthetic aperture radar (SAR) Processor from Gamma Remote Sensing, except for autofocus and azimuth compression, for which we use the pseudo inverse Fourier transform instead of regular range-doppler focusing (Hyung-Sup Jung, personal communication, 2012). For each track, we obtain small spatial baseline interferograms with perpendicular baselines less than 200 m using the JPL/Caltech ROI_PAC software (see Figures S5 and S6 in the supporting information for the networks of interferograms). We use the DORIS orbits and the 3 arc sec SRTM digital elevation model, interpolated to 1 arc sec spacing, to simulate and remove the phase due to the topography and earth curvature from each interferogram. We take 8 looks in range and 40 looks in azimuth direction and filter the interferograms using a Goldstein filter. We coregister the multilooked and filtered interferograms to a master SAR image. We unwrap the coregistered interferograms using Snaphu [*Chen and Zebker*, 2001], evaluate the phase consistency for triplets of interferograms, and correct for phase-unwrapping errors using the approach of *Fattahi* [2015].

We then invert the network of interferograms to obtain the phase history at each epoch relative to the first acquisition [*Berardino et al.*, 2002]. We use connected networks of interferograms (Figures S5 and S6) so that a bias can only be caused by phase inconsistencies, e.g., due to filtering [*Agram and Simons*, 2015], phase decorrelation, and/or phase-unwrapping errors. To ensure unbiased estimation of the phase history, we evaluate

the temporal coherence, which represents the residual of the difference of unwrapped interferometric phases used in the inversion and the reconstructed interferograms obtained from the estimated phase history, and mask out the incoherent pixels using a threshold of 0.7 [*Pepe et al.*, 2006]. In the time domain we then correct for the local oscillator drift of the ASAR instrument [*Marinkovic and Larsen*, 2013; *Fattahi and Amelung*, 2014] and for topographic residuals [*Fattahi and Amelung*, 2013]. We use the ERA-Interim global atmospheric reanalysis model [*Dee et al.*, 2011] to correct the stratified tropospheric delay [*Jolivet et al.*, 2014b]. The corrected phase history after conversion to change in distance between the ground and the satellite represents the ground displacement time series in radar line of sight (LOS) direction.

For each pixel we estimate the LOS velocity, which is the slope of the linear fit to the displacement time series. The displacement is a relative measurement with respect to a reference pixel on the same track. Accordingly, the LOS velocity field shows the relative velocity between any pair of coherent pixels. We concatenate the velocity fields of adjacent tracks by estimating a constant offset as the median of the differences of the velocity fields in the overlapping areas. The median is less sensitive to localized residual tropospheric delays (not represented by the ERA-I model) than the mean. After adjusting the adjacent tracks, we use for the overlapping areas the average velocity of the two tracks.

For the 2008 $M > 6$ earthquakes close to Pishin we eliminated the postearthquake acquisitions on tracks 213 and 485 because the coseismic displacements violate the assumption of linear deformation.

The uncertainties of the LOS velocity field are dominated by the spatially variable residual stochastic tropospheric delay. They are given relative to a reference pixel in each track in Figure 6b of *Fattahi and Amelung* [2015]. The averaged uncertainties are given as a function of distance in their Figure 7. The velocity uncertainty increases from ~2 mm/yr over 100 km to ~4 mm/yr over 400 km distance. In the remainder of this paper all uncertainties are averaged uncertainties inferred from this Figure.

4. Modeling Approach

We assume that the relative plate motion is accommodated by movements along one or more vertical strike-slip faults that are either locked or creeping from the surface to some depth. We model a fault as a combination of a buried infinite screw dislocation in an elastic half-space representing interseismic strain accumulation along a locked fault [*Savage and Burford*, 1973] and a dislocation extending from the surface to a given depth, representing the accommodation of strain by shallow creep [*Segall*, 2010, equation 2.30]. The fault-parallel surface velocity due to slip along N parallel faults is given by

$$v_{\parallel}(x) = \sum_{i=1}^{N} \frac{S_i}{\pi} \arctan\left(\frac{x - f_i}{D_i}\right) + \frac{C_i}{\pi} \arctan\left(\frac{E_i}{x - f_i}\right) \tag{1}$$

with S_i the deep fault slip rate (also simply referred to as slip rate), D_i the locking depth, C_i the creep rate ($0 \leq C_i \leq S_i$), E_i the creep extent of the ith fault at location f_i, and x the distance from the first fault, for which $f_1 = 0$ (see Figure S7 for an example). A fault creeping at the deep slip rate throughout the crust is given by $C = S$ and $E = D$, and $v(x)$ approaches a Heaviside function scaled by the slip rate.

We use a Bayesian approach to obtain the range of possible models of interseismic strain accumulation and release. The posterior probability density function (PDF) of the model parameters, $p(\boldsymbol{m}|\boldsymbol{d})$, is defined as

$$p(\boldsymbol{m}|d) \sim p(\boldsymbol{m}) \exp\left[(\boldsymbol{d} - \boldsymbol{p})^T C^{-1}(\boldsymbol{d} - \boldsymbol{p})\right] \tag{2}$$

with $\boldsymbol{d}$ and $\boldsymbol{p}$ vectors containing the observations and model predictions, C^{-1} the inverse of the covariance matrix of the data, and $p(\boldsymbol{m})$ the prior PDF of the model parameters. We use uniform prior distributions and construct the covariance matrix based on *Fattahi and Amelung* [2015, equation 14] using their averaged uncertainties as a function of distance. We sample the posterior PDFs using a Gibbs sampling algorithm with 200,000 sweeps over the model parameters at a critical temperature of one [*Brooks and Neil Frazer*, 2005].

5. Results

The relative InSAR LOS velocity field for the plate boundary zone (Figure 1b) shows relative lengthening of the distance between the satellite and the ground of the eastern part of the study area with respect to the western part by 8–15 mm/yr, consistent with the motion of the Indian plate relative to Eurasia toward the

Table 1. The Best Fitting Model Parameters for the Transects AA' and BB' (Figures 2a and 2b)[a]

Profile	Fault	S (mm/yr)	D (km)	C (mm/yr)	E (km)	f (k)
AA'	Chaman	6.1 ± 1.1	10[b]	5[b]	7.2 ± 2.0	60[b]
	Arbitrary	6.2 ± 1.1	10[b]	0[b]	0[b]	125[b]
BB'	Chaman	8.1 ± 3.2	27.2 ± 8.7	2.8 ± 0.4	6.1 ± 2.2	65[b]
	Ghazaband	16.3 ± 2.3	10.6 ± 2.3	0[b]	0[b]	105.0 ± 0.5

[a]S: slip rate, D: locking depth, C: creep rate, E: creep extent, and f: fault location from beginning of the profile. 1 sigma uncertainties were estimated using a Gibbs sampling approach. Parameters without uncertainty were fixed.
[b]Denotes ad hoc selected model parameters. See supporting information Figures S2 and S3 for the plots of marginal posterior density distribution of estimated parameters.

Himalaya. Cold colors (blue) indicate ground movements away from the satellite relative to warmer colors (red). The shortening of the distance to the satellite north of the Hoshab Fault (red colors) relative to the area south of it may in part represent strain accumulation along the oblique-slip crustal faults in the Makran Range and along the subduction megathrust.

5.1. Strain Accumulation From Transects

Two fault-perpendicular transects in the central Chaman Fault system with a width of ~40 km show relative LOS velocities of 7 ± 3 mm/yr and 12 ± 3.2 mm/yr, corresponding to fault-parallel velocities of 14 ± 6 and 30 ± 6.4 mm/yr, respectively, using the local fault strike (Figures 1a and 1b). The uncertainties apply to the total transect lengths of 140 and 160 km, respectively. For comparison, the resolved fault-parallel components of the relative plate motion vector are 25 and 28 mm/yr, respectively. Discontinuities in LOS velocity at the location where the transects cross the Chaman Fault indicate surface creep. The decreases in LOS velocity at 30–40 km distance along AA' and at 110–120 km distance along BB' likely represent land subsidence due to groundwater withdrawal. The decrease in LOS velocity at 10–30 km and 150–170 km distance along BB' could represent vertical deformation related to thrust faults.
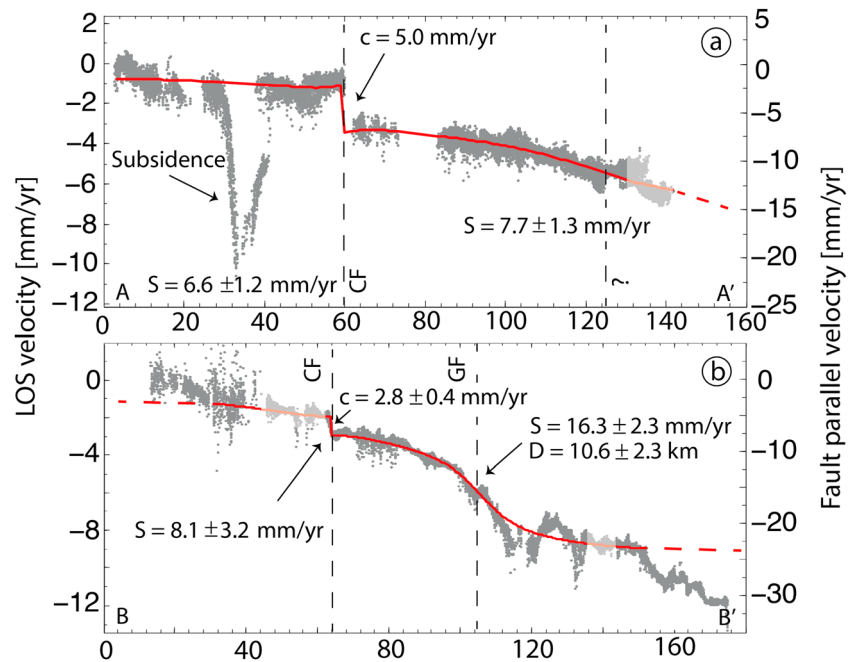
Figure 2. Transects of the LOS velocity field perpendicular to (a) the Chaman Fault (AA') and (b) the Ghazaband Fault (BB') (oriented N55.5 W and N67°W, respectively). The uncertainties over the transect lengths (140 and 160 km) are 3 and 3.2 mm/yr LOS. Light grey: averaged LOS velocities from two overlapping tracks. Red lines in (Figures 2a and 2b): best fitting models (see text). For the two central Chaman Fault transects, we project the LOS velocity, v, to fault-parallel velocities, $v_{||}$, as $v_{||} v/(\sin(az)\cos(h)\sin(\vartheta) - \cos(az)\sin(h)\sin(\vartheta))$ where az is the local fault strike (34.5° for transect AA' and 22.75° for transect BB'), h is the satellite heading angle (347°), and ϑ is the average radar incidence angle (41° for the ASAR IS6 beam).
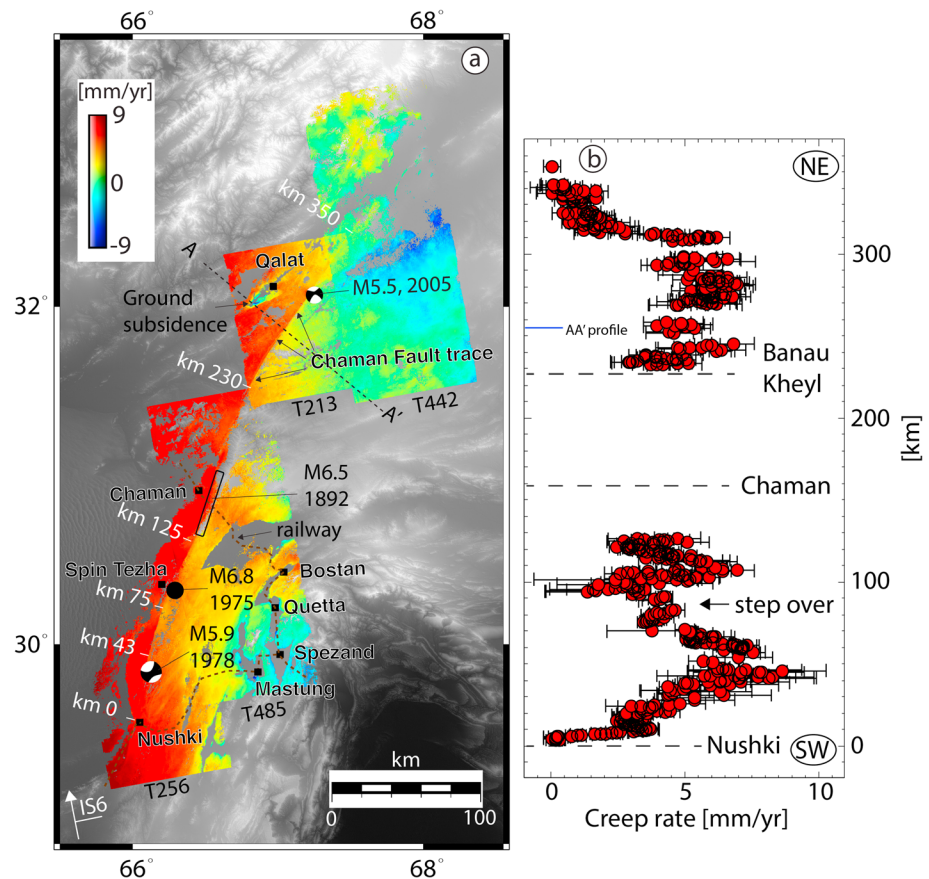
Figure 3. (a) LOS velocity field for the Central Chaman Fault and (b) surface creep rates for 1 km intervals from the city of Nushki toward NNW. Figure 3a is the same as Figure 1b except with different color scales and except for track 213, for which we have omitted the frames with fewer acquisitions. See supporting information Figure S4 for a descending track and Figures S5 and S6 for the interferogram networks. The earthquake locations for events without CMT solution are from *Ambraseys and Bilham* [2003].

We assume that the deformation along transect BB′, which exhibits an arctangent pattern typical for interseismic strain accumulation, is due to two faults, one of which is creeping at the surface. We infer the posterior PDFs for seven model parameters, the slip rate, locking depth, location of fault 1 (Ghazaband), the slip rate, creep rate, creep extent, and locking depth of fault 2 (Chaman), and for a constant offset. The model Chaman Fault coincides with the LOS velocity discontinuity. We mask out the signals due to subsidence and due to suspected thrust faulting and subsample the data by averaging the LOS velocities over 1 km intervals along the transect (supporting information Figure S1). We find slip rates of 8.1 ± 3.2 and 16.3 ± 2.3 for the Chaman and Ghazaband Faults, respectively, a locking depth of 10.6 ± 2.3 km for the Ghazaband Fault, and a creep rate of 2.8 ± 0.4 mm/yr for the Chaman Fault (Table 1). The locking depth and creep extent of the Chaman Fault are not constrained because of trade-offs with the other model parameters (E1 and D1 in the supporting information Figure S2).

For transect AA′ which does not show any arctan pattern we consider a two-fault model consisting of a fault with a surface creep rate of 5 mm/yr and a locking depth of 10 km and an arbitrary fault at 125 km distance with a locking depth of 10 km (although the lack of a surface expression for a fault at 80–140 km distance suggests diffuse deformation). We find a slip rate of 6.6 ± 1.2 mm/yr for the Chaman Fault. Models with a higher locking depth for the arbitrary fault and models with two arbitrary faults give similar but lower slip rates for the Chaman Fault (Table S1). The two southern transects showing strain accumulation across the Panjgur Fault and surface creep across the Hoshab Fault northeast of the 2013 rupture are discussed in the supporting information S1.

5.2. Shallow Creep Along the Chaman Fault

The discontinuity in the LOS velocity field across the Chaman Fault is evidence for shallow fault creep (Figure 2a). The descending LOS velocity field does not show this signal (supporting information Figure S4)

because a fault-perpendicular looking radar is insensitive to fault-parallel displacements. To estimate along-strike variations of the surface creep rate, we consider seven sections with different strikes and $1\,km^2$ squares at distances of 0.3 km from both sides of the fault. The creep rate is given by the difference in the LOS velocity averages; the variance of the creep rate is given by the sum of the variances. We project the LOS creep rates to fault-parallel creep rates assuming horizontal deformation. The surface creep rate increases from no creep at Nushki to 8.1 ± 2 mm/yr at 42–45 km distance and shows along-strike variability (Figure 3b). The creep rate between 125 and 230 km distance is not determined because of a lack of interferometric coherence near the fault. The total length of the creeping segment is 340 km.

6. Discussion

6.1. Slip Rates

Our modeling shows that at 29 N the shear from the relative plate motion is accommodated by both the Chaman and Ghazaband Faults with estimated slip rates of 8.1 ± 3.2 and 16.3 ± 2.3 mm/yr, respectively (transect BB'). At about 32 N the slip rate of the Chaman Fault is 6.6 ± 1.2 mm/yr (transect AA'). In the following we use a slip rate of 8 mm/yr (within the 2 sigma confidence interval of the transect AA' estimate). This rate is consistent with the rate of $8.5^{+1.8}_{-1.7}$ mm/yr of *Szeliga et al.* [2012] from 5 years of GPS observations for a profile near Chaman City and the observation that a campaign GPS station in Kabul accounts for 75% of the India-Eurasia motion, leaving 25% for the Chaman Fault to the west [*Szeliga et al.*, 2012]. However, it is lower than the geological slip rate of 33.3 ± 3 mm/yr [*Ul-Hadi et al.*, 2013], which is inferred from surface exposure ages of an offset alluvial fan near the town of Chaman. Possible explanations for this discrepancy are that either the fault has recently slowed or that the age estimate of the fan is biased by surface erosion [*Behr et al.*, 2010].

6.2. Creeping Segment

We have identified a 340 km long creeping segment along the Chaman Fault (Figure 2). In the past 100+ years this segment was ruptured by three significant earthquakes, in 1892 by a $M_s6.5$ near Chaman City (associated with 65–80 cm over 30–60 km), in 1975 by a $M_s6.8$ near Spin Tezha, and in 1978 by a $M_w5.9$ near Nushki (Figure 2a) [*Ambraseys and Bilham*, 2003]. The coincidence of fault creep and fault rupture puts the Chaman Fault on the growing list of continental strike-slip faults with partially coupled segments [*Jolivet et al.*, 2014a; *Avouac*, 2015; *Chaussard et al.*, 2015] and suggests that the overall frictional behavior of the fault varies over time as documented elsewhere [*Çakir et al.*, 2012; *Kaneko et al.*, 2013; *Cetin et al.*, 2014].

6.3. Seismic Hazard

We use the inferred slip rate, locking depth, and creep information to obtain first-order estimates of the slip deficits and of the seismic potential of the Ghazaband Fault, of the creeping segment of the Chaman Fault, and of the Northern Chaman Fault. For the conversion from slip to seismic moment we use a rigidity of 30×10^9 nm. Given the model assumptions (vertical faults, 2-D geometry) and the lack of InSAR coverage of the northern Chaman Fault, we recognize that the following discussion represents a simplified interpretation of this complex area.

6.3.1. Ghazaband Fault

There was no major earthquake on the Ghazaband Fault since at least 1870. The strain accumulation rate of 16 mm/yr below a locking depth of 10.6 km is equivalent to an $M_w7.3$ earthquake every 100 years (for a length of 250 km). The four $M_w > 5$ earthquakes in the 40 years long global centroid moment tensor (CMT) catalog in the area ($M_w6.1$ and $M_w5.3$ in 1990, $M_w5.6$ in 1993, and $M_w5.5$ in 2007) account for only 5% of the accumulated moment. The accumulated moment deficit makes the Ghazaband Fault one of the most hazardous faults in the plate boundary zone. Here we follow the notion that the 1935 $M7.7$ Quetta earthquake did not rupture this fault [*Ambraseys and Bilham*, 2003; *Armbruster et al.*, 1980] inferred from the lack of reports about railroad damages at the fault crossing at 29.5°N (railroad damages were reported east near Mastung [*Armbruster et al.*, 1980]). For an alternative opinion see *Szeliga et al.* [2012].

6.3.2. Chaman Fault Creeping Segment

For this 340 km long segment (29.5°N to 32.3°N), the tectonic loading rate of 8 mm/yr corresponds to 1 m of slip accumulated over the 124 years since the 1892 earthquake. About one third of the slip has been accommodated seismically (the summed moment of the three earthquakes corresponds to an averaged slip of 0.37 m for a locking depth of 10.6 km). As our data do not resolve the coupling coefficient, we assume that

one quarter of the slip is accommodated aseismically (inferred from the observation that the surface creep is about half the loading rate and assuming a creep extent of half the locking depth). This leaves 0.38 m of potential slip available for the next rupture, corresponding to a moment magnitude of M_w7.0 using a locking depth of 10.6 km. Hence, the creeping segment has the potential to generate a major earthquake. Here we have assumed that creep has been constant over the time period considered and we have ignored aftershocks and afterslip.

6.3.3. Northern Chaman Fault

The moment deficit along the 343 km long fault segment (32.3°N to 35.0°N) is of interest because the last major earthquake in 1505 near Paghman caused significant damage in the city of Kabul [*Quittmeyer and Jacob*, 1979; *Ambraseys and Bilham*, 2014]. As it is not covered by InSAR we use the slip rate and locking depths inferred farther south. For a slip rate of 8 mm/yr the slip available is 4 m, corresponding to an M_w7.6. This explains the lack of major earthquakes over the past 500 years but does not imply a low hazard. If there is additional creep along this segment or if some of the deformation is accommodated along the Gardez fault farther to the east, the slip available for the next earthquake is even less.

6.3.4. Geodynamical Implications

Our study has shown that the Chaman Fault, which is the most prominent tectonic structure in the plate boundary zone, accounts with a slip rate of 8 ± 3.1 mm/yr only for ~30% of the shear component of the relative plate motion between India and Eurasia of 25 mm/yr. As the relative motion between the Helmand block and Eurasia is negligible [*Mohadjer et al.*, 2010; *Walpersdorf et al.*, 2014], the remaining ~70% must be accommodated east of the Chaman Fault. South of 30.5°N it is accommodated by the Ghazaband Fault; the combined slip rate of the two faults is 24 ± 4 mm/yr. North of this latitude, the Katawaz block [*Reynolds et al.*, 2015] gives rise to a local zone of convergence because it is oriented perpendicular to the plate motion vector. The surface expression of this convergence is the thick-folded sediment layers in the Sulaiman Lobe. Our results imply that ~70% of the relative plate motion is accommodated in this convergence zone.

7. Conclusions

The Envisat InSAR observations corrected for local oscillator drift, topographic residuals, and stratified tropospheric delay show that the Chaman Fault does not act as the sole transform boundary between stable India and Eurasia but accommodates only ~8 mm/yr of the relative motion between the two plates. The plate boundary deformation is accommodated over a wider zone with the Ghazaband Fault accounting for ~16 mm/yr. North of the Ghazaband Fault, the deformation must be accommodated by faults to the south and east of the Katawaz block. Along a 340 km long segment of the Chaman Fault the deformation is partly accommodated by shallow fault creep with maximum surface creep rate of ~8 mm/yr.

References

Agram, P. S., and M. Simons (2015), A noise model for InSAR time series, *J. Geophys. Res. Solid Earth*, *120*, 2752–2771, doi:10.1002/2014JB011271.

Ambraseys, N., and R. Bilham (2003), Earthquakes and associated deformation in northern Baluchistan 1892–2001, *Bull. Seismol. Soc. Am.*, *93*(4), 1573–1605.

Ambraseys, N., and R. Bilham (2014), The tectonic setting of Bamiyan and seismicity in and near Afghanistan for the past twelve centuries, in *After the Destruction of Giant Buddha Statues in Bamiyan (Afghanistan) in 2001*, pp. 101–152, Springer, Berlin.

Armbruster, J., L. Seeber, R. C. Quirtmeyer, and A. Farah (1980), Seismic network data from Quetta, Pakistan: The Chaman Fault and the fault related to the 30 May 1935 earthquake, in *Intern. Commit. Geodynamics, Grp 6, Mtg. Peshawar*, vol. 13, Spec. Issue, Geol Bull Univ. Pishawar.

Avouac, J.-P. (2015), From geodetic imaging of seismic and aseismic fault slip to dynamic modeling of the seismic cycle, *Annu. Rev. Earth Planet. Sci.*, *43*(1), 233–271, doi:10.1146/annurev-earth-060614-105302.

Avouac, J.-P., F. Ayoub, S. Wei, J.-P. Ampuero, L. Meng, S. Leprince, R. Jolivet, Z. Duputel, and D. Helmberger (2014), The 2013, M_w 7.7 Balochistan earthquake, energetic strike-slip reactivation of a thrust fault, *Earth Planet. Sci. Lett.*, *391*, 128–134, doi:10.1016/j.epsl.2014.01.036.

Behr, W. M., et al. (2010), Uncertainties in slip-rate estimates for the Mission Creek strand of the southern San Andreas fault at Biskra Palms Oasis, southern California, *Geol. Soc. Am. Bull.*, *122*(9–10), 1360–1377.

Berardino, P., G. Fornaro, R. Lanari, S. Member, and E. Sansosti (2002), A new algorithm for surface deformation monitoring based on small baseline differential SAR interferograms, *IEEE Trans. Geosci. Remote Sens.*, *40*(11), 2375–2383.

Bernard, M., B. Shen-Tu, W. E. Holt, and D. M. Davis (2000), Kinematics of active deformation in the Sulaiman Lobe and Range, Pakistan, *J. Geophys. Res.*, *105*(B6), 13,253–13,279, doi:10.1029/1999JB900405.

Brooks, B. A., and L. Neil Frazer (2005), Importance reweighting reduces dependence on temperature in Gibbs samplers: An application to the coseismic geodetic inverse problem, *Geophys. J. Int.*, *161*(1), 12–20, doi:10.1111/j.1365-246X.2005.02573.x.

Çakir, Z., S. Ergintav, H. Özener, U. Dogan, A. M. Akoglu, M. Meghraoui, and R. Reilinger (2012), Onset of aseismic creep on major strike-slip faults, *Geology*, *40*(12), 1115–1118.

Cetin, E., Z. Cakir, M. Meghraoui, S. Ergintav, and A. Akoglu (2014), Extent and distribution of aseismic slip on the Ismetpasa segment of the North Anatolian Fault (Turkey) from persistent scatterer InSAR, *Geochem. Geophys. Geosyst.*, 15, 2883–2894, doi:10.1002/2014GC005307.

Chaussard, E., R. Bürgmann, H. Fattahi, R. M. Nadeau, T. Taira, C. W. Johnson, and I. Johanson (2015), Potential for larger earthquakes in the East San Francisco Bay Area due to the direct connection between the Hayward and Calaveras Faults, *Geophys. Res. Lett.*, 1–8, 2734–2741, doi:10.1002/2015GL063575.

Chen, C. W., and H. A. Zebker (2001), Two-dimensional phase unwrapping with use of statistical models for cost functions in nonlinear optimization, *J. Opt. Soc. Am. A*, 18(2), 338–351, doi:10.1364/JOSAA.18.000338.

Dee, D. P., et al. (2011), The ERA-Interim reanalysis: Configuration and performance of the data assimilation system, *Q. J. R. Meteorol. Soc.*, 137(656), 553–597, doi:10.1002/qj.828.

Fattahi, H. (2015), Geodetic imaging of tectonic deformation with InSAR, Univ. of Miami.

Fattahi, H., and F. Amelung (2013), DEM error correction in InSAR time series, *IEEE Trans. Geosci. Remote Sensing*, 51(7), 4249–4259, doi:10.1109/tgrs.2012.2227761.

Fattahi, H., and F. Amelung (2014), InSAR uncertainty due to orbital errors, *Geophys. J. Int.*, 199(1), 549–560, doi:10.1093/gji/ggu276.

Fattahi, H., and F. Amelung (2015), InSAR bias and uncertainty due to the systematic and stochastic tropospheric delay, *J. Geophys. Res. Solid Earth*, 120, 1–16, doi:10.1002/2015JB012419.

Fattahi, H., F. Amelung, E. Chaussard, and S. Wdowinski (2015), Coseismic and postseismic deformation due to the 2007 $M5.5$ Ghazaband fault earthquake, Balochistan, Pakistan, *Geophys. Res. Lett.*, 42, 3305–3312, doi:10.1002/2015GL063686.

Furuya, M., and S. P. Satyabala (2008), Slow earthquake in Afghanistan detected by InSAR, *Geophys. Res. Lett.*, 35, doi:10.1029/2007GL033049.

Haq, S., and D. M. Davis (1997), Oblique convergence and the lobate mountain belts of western Pakistan, *Geology*, 25(1), 23–26.

Jolivet, R., M. Simons, P. S. Agram, Z. Duputel, and Z. Shen (2014a), Aseismic slip and seismogenic coupling along the central San Andreas Fault, *Geophys. Res. Lett.*, 42, 1–10, doi:10.1002/2014GL062222.We.

Jolivet, R., P. S. Agram, N. Y. Lin, M. Simons, M. Doin, G. Peltzer, and Z. Li (2014b), Improving InSAR geodesy using Global Atmospheric Models, *J. Geophys. Res. Solid Earth*, 119, 2324–2341, doi:10.1002/2013JB010588.

Kaneko, Y., Y. Fialko, D. T. Sandwell, X. Tong, and M. Furuya (2013), Interseismic deformation and creep along the central section of the North Anatolian Fault (Turkey): InSAR observations and implications for rate-and-state friction properties, *J. Geophys. Res. Solid Earth*, 118, 316–331, doi:10.1029/2012JB009661.

Lawrence, R. D., S. H. Khan, and T. Nakata (1992), Chaman Fault, Pakistan-Afghanistan, *Ann. Tectonicae*, 6, 196–223.

Marinkovic, P., and Y. Larsen (2013), Consequences of long-term ASAR local oscillator frequency decay—An empirical study of 10 years of data, in *Living Planet Symp.*, Edinburgh, U. K.

Mohadjer, S., et al. (2010), Partitioning of India-Eurasia convergence in the Pamir-Hindu Kush from GPS measurements, *Geophys. Res. Lett.*, 37, L04305, doi:10.1029/2009GL041737.

Molnar, P., and K. E. Dayem (2010), Major intracontinental strike-slip faults and contrasts in lithospheric strength, *Geosphere*, 6(4), 444–467.

Pepe, A., R. Lanari, and S. Member (2006), On the extension of the minimum cost flow algorithm for phase unwrapping of multitemporal differential SAR interferograms, *IEEE Trans. Geosci. Remote Sens.*, 44(9), 2374–2383.

Quittmeyer, R. C., and K. H. Jacob (1979), Historical and modern seismicity of Pakistan, Afghanistan, northwestern India, and southeastern Iran, *Bull. Seismol. Soc. Am.*, 69(3), 773–823.

Reynolds, K., A. Copley, and E. Hussain (2015), Evolution and dynamics of a fold-thrust belt: The Sulaiman Range of Pakistan, *Geophys. J. Int.*, 201, 683–710, doi:10.1093/gji/ggv005.

Savage, J. C., and R. O. Burford (1973), Geodetic determination of relative plate motion in central California, *J. Geophys. Res.*, 78(5), 832–845, doi:10.1029/JB078i005p00832.

Segall, P. (2010), *Earthquake and Volcano Deformation*, Princeton Univ. Press.

Szeliga, W., R. Bilham, D. Schelling, D. M. Kakar, and S. Lodi (2009), Fold and thrust partitioning in a contracting fold belt: Insights from the 1931 Mach earthquake in Baluchistan, *Tectonics*, 28(5), doi:10.1029/2008TC002265.

Szeliga, W., R. Bilham, D. M. Kakar, and S. H. Lodi (2012), Interseismic strain accumulation along the western boundary of the Indian subcontinent, *J. Geophys. Res.*, 117, B08404, doi:10.1029/2011JB008822.

Thatcher, W. (2009), How the continents deform: The evidence from tectonic geodesy *, *Annu. Rev. Earth Planet. Sci.*, 37(1), 237–262, doi:10.1146/annurev.earth.031208.100035.

Ul-Hadi, S., S. D. Khan, L. A. Owen, A. S. Khan, K. A. Hedrick, and M. W. Caffee (2013), Slip-rates along the Chaman fault: Implication for transient strain accumulation and strain partitioning along the western Indian plate margin, *Tectonophysics*, 608, 389–400, doi:10.1016/j.tecto.2013.09.009.

Walpersdorf, A., et al. (2014), Present-day kinematics and fault slip rates in eastern Iran, derived from 11 years of GPS data, *J. Geophys. Res. Solid Earth*, 119, 1359–1383, doi:10.1002/2013JB010620.

Yeats, R. (2012), *Active Faults of the World*, Cambridge Univ. Press.

Yeats, R. S., R. D. Lawrence, S. Jamil-Ud-Din, and S. H. Khan (1979), Surface effects of the 16 March 1978 earthquake, Pakistan-Afghanistan border, *Geodyn. Pakistan*, 359–361.